



Structural analysis of substrate-mimicking inhibitors in complex with *Neisseria meningitidis* 3-deoxy-D-arabino-heptulosonate 7-phosphate synthase – The importance of accommodating the active site water

Logan C. Heyes^a, Sebastian Reichau^{a,1}, Penelope J. Cross^a, Geoffrey B. Jameson^b, Emily J. Parker^{a,*}

^a Biomolecular Interaction Centre and Department of Chemistry, University of Canterbury, Christchurch, New Zealand

^b Institute of Fundamental Sciences, Massey University, Palmerston North, New Zealand

ARTICLE INFO

Article history:

Available online 27 August 2014

Keywords:

DAH7PS
DAHPS
Aromatic amino acids
Shikimate pathway
Oxocarbenium ion
Enzyme inhibitors
Meningitis

ABSTRACT

3-Deoxy-D-arabino-heptulosonate 7-phosphate synthase (DAH7PS) catalyses the first committed step of the shikimate pathway, which produces the aromatic amino acids as well as many other aromatic metabolites. DAH7PS catalyses an aldol-like reaction between phosphoenolpyruvate and erythrose 4-phosphate. Three phosphoenolpyruvate mimics, (*R*)-phospholactate, (*S*)-phospholactate and vinyl phosphonate [(*E*)-2-methyl-3-phosphonoacrylate], were found to competitively inhibit DAH7PS from *Neisseria meningitidis*, which is the pathogen responsible for bacterial meningitis. The most potent inhibitor was the vinyl phosphonate with a K_i value of $3.9 \pm 0.4 \mu\text{M}$. We report for the first time crystal structures of these compounds bound in the active site of a DAH7PS enzyme which reveals that the inhibitors bind to the active site of the enzyme in binding modes that mimic those of the predicted oxocarbenium and tetrahedral intermediates of the enzyme-catalysed reaction. Furthermore, the inhibitors accommodate the binding of a key active site water molecule. Together, these observations provide strong evidence that this active site water participates directly in the DAH7PS reaction, enabling the facial selectivity of the enzyme-catalysed reaction sequence to be delineated.

© 2014 Elsevier Inc. All rights reserved.

1. Introduction

3-Deoxy-D-arabino-heptulosonate 7-phosphate synthase (DAH7PS) catalyses the first committed step of the shikimate pathway, which is responsible for the biosynthesis of the aromatic amino acids and other important aromatic metabolites in plants and microorganisms [1,2]. In mammals these essential metabolites are obtained from dietary sources, and the enzymes of the shikimate pathway are absent. Therefore, the enzymes of this pathway have been

Abbreviations: BTP, 1,3-bis(tris(hydroxymethyl)methylamino)propane; DAH7PS, 3-deoxy-D-arabino-heptulosonate 7-phosphate synthase; E4P, D-erythrose 4-phosphate; EDTA, ethylenediaminetetraacetic acid; LE, ligand efficiency; NCS, non-crystallographic symmetry; NMR, nuclear magnetic resonance; PEP, phosphoenolpyruvate; RMSD, root-mean-square deviation; TMAO, trimethyl-amino-N-oxide; Tris, tris(hydroxymethyl)aminomethane.

* Corresponding author. Address: Department of Chemistry, University of Canterbury, Private Bag 4800, Christchurch, New Zealand. Fax: +64 3 364 2110.

E-mail address: emily.parker@canterbury.ac.nz (E.J. Parker).

¹ Current address: Technische Universität Berlin, Fakultät II Mathematik und Naturwissenschaften, Institut für Chemie / OC / Biologische Chemie, Müller-Breslau-Straße 10, L3, 10623 Berlin, Germany.

<http://dx.doi.org/10.1016/j.bioorg.2014.08.003>

0045-2068/© 2014 Elsevier Inc. All rights reserved.

identified as promising targets for the development of new anti-bacterial therapeutics [3–5].

DAH7PS catalyses the condensation between D-erythrose 4-phosphate (E4P, **2**) and phosphoenol-pyruvate (PEP, **1**) to generate DAH7P (**3**, Fig. 1). Many of the key mechanistic details of the reaction have been elucidated through various labelling, structural and alternative-substrate studies [3,6–12]. The ordered sequential reaction proceeds stereospecifically with respect to both substrates, with the *si* face of PEP attacking the *re* face of E4P. The aldol-like reaction takes place with cleavage of the C–O bond of the phosphate group of PEP, requiring water to act as a co-substrate. The initial nucleophilic attack of PEP on E4P is predicted to be promoted by coordination of the E4P aldehydic oxygen to the essential divalent metal ion, giving an oxocarbenium ion intermediate **4** (Fig. 1) [3,6]. The addition of an active site nucleophilic water results in a phosphohemiketal tetrahedral intermediate **5**, which forms acyclic DAH7P on the elimination of phosphate. The stereochemistry of the tetrahedral intermediate **5**, which is lost on the elimination of phosphate, is determined by the face of the oxocarbenium ion **4** that is attacked by the nucleophilic water. Therefore, the ability of the active site to accommodate and

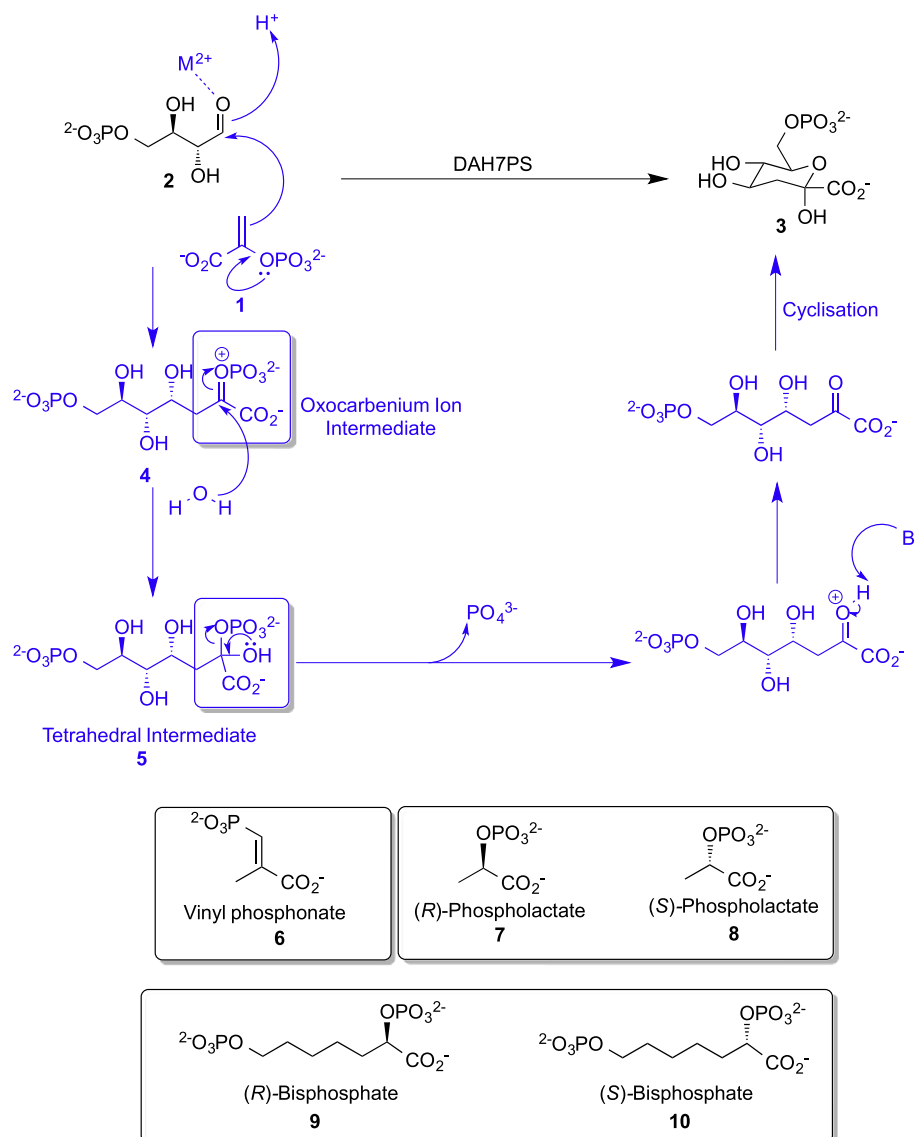


Fig. 1. The overall DAH7PS catalysed reaction showing the likely mechanism via oxocarbenium ion and tetrahedral intermediates (in blue). Compounds **6–10** have been shown to act as inhibitors of the DAH7PS enzymes from *Escherichia coli* or *Mycobacterium tuberculosis*.

activate a water molecule is an important aspect of DAH7PS catalysis and, furthermore, may have implications for inhibitor design [3,13].

DAH7PS enzymes have been structurally and functionally characterised from a variety of sources [6,13–19]. While all known enzymes have similar active site architectures supporting a common catalytic mechanism and share a common (β/α)₈-barrel core, there is considerable sequence divergence between enzymes from different sources leading to the classification of DAH7PS enzymes into two types [20]. Type I enzymes are further divided into type I α and type I β subfamilies, which differ in sequence and their allosteric regulatory machinery. The only structurally characterised type II enzyme is from *Mycobacterium tuberculosis* [16,21].

Active site inhibitors have been previously reported for the phenylalanine-sensitive type I α DAH7PS from *Escherichia coli* (EcoDAH7PS) and the type II enzyme from *M. tuberculosis* (MtuDAH7PS) [3,12,22–24]. PEP-like analogues were found to inhibit EcoDAH7PS, with the most potent inhibitor being the vinyl phosphonate, (*E*)-2-methyl-3-phosphonoacrylate **6**, followed by the (*R*)-phospholactate **7** [23]. (*S*)-Phospholactate **8** was the poorest inhibitor. The rationale for a ten-fold difference in potency of the two phospholactate

stereoisomers is not clear, as no structures of the inhibited enzymes were determined, but may relate to the stereochemistry of the transient phosphohemiketal tetrahedral intermediate **5**. The vinyl phosphonate **6** was found to have a *K_i* of $4.7 \pm 0.7 \mu\text{M}$, which approaches the *K_m* for PEP of $2 \mu\text{M}$ for this enzyme [23]. Inhibition studies on the type II MtuDAH7PS were carried out using extended (*R*)- and (*S*)-phospholactates of variable chain length bearing an additional phosphate moiety in order to better mimic the key functionality of the tetrahedral intermediate (bisphosphates **9** and **10**) [3,24]. In each case the compounds bearing (*R*)-configuration were found to inhibit enzymatic activity more potently than the respective (*S*)-enantiomers. The seven-carbon containing (*R*)-bisphosphate **9** had a *K_i* value of $0.36 \pm 0.05 \mu\text{M}$, consistent with this compound significantly out-competing the natural substrate PEP (*K_m^{PEP}* of $37 \mu\text{M}$) [3,24].

The genome of *Neisseria meningitidis*, the causative agent of pyogenic meningitis and meningococcal septicaemia, encodes a single type I α DAH7PS (*NmeDAH7PS*) [17,25]. The crystal structure of *NmeDAH7PS*, which was recently determined in our laboratory, revealed that the active site of *NmeDAH7PS* shares many similarities to the DAH7PS from *E. coli* [33]. The active site Mn²⁺

is coordinated in a trigonal–bipyramidal fashion by four conserved protein residues, Cys63, His270, Asp304 and Asp324 [17], leaving one coordination site available for the aldehyde moiety of E4P. PEP binding occurs through interaction with the highly conserved residues Arg167, Arg236, Lys188, Arg94 and Lys99. The predicted E4P binding site consists of a highly conserved motif involving the residues Lys99, Pro100, Arg101 and Thr102.

Here we examine the inhibition of *Nme*DAH7PS by the active site directed PEP-mimicking inhibitors **6**, **7** and **8** in order to assess their efficacies against a DAH7PS enzyme from an important pathogen. Furthermore, we report for the first time crystal structures of a DAH7PS, here *Nme*DAH7PS, in complex with each of these inhibitors, revealing that these inhibitors do accurately mimic the binding modes predicted for the oxocarbenium ion **4** and tetrahedral intermediates **5**, along with the co-coordination of a water molecule. Our findings allow refinement of the DAH7PS mechanism, aid the identification of the nucleophilic water in this type I α enzyme and guide further structure-based inhibitor design of this enzyme.

2. Experimental

2.1. Inhibitor synthesis

(*R*)-Phospholactate **7**, (*S*)-phospholactate **8** and the vinyl phosphonate **6** were synthesised according to the previously reported methods [23]. Concentration determination of the vinyl phosphonate **6** was achieved by comparison of signal integrals from ^{31}P NMR spectroscopy using 85% phosphoric acid as a standard at sufficiently long relaxation times. Phospholactate concentrations were determined via Lanzetta assay for phosphate detection as previously described [3,26].

2.2. Inhibition assays

Enzyme activity was measured by monitoring the loss of absorbance at 232 nm indicating the consumption of PEP (Sigma–Aldrich). Assays were carried out in 50 mM bis(tris(hydroxymethyl) methylamino)propane (BTP) buffer at pH 6.8 with 10 μM ethylenediaminetetraacetic acid (EDTA). The buffer was made up in ultrapure water that had been treated with Chelex resin. E4P was synthesised as reported previously from glucose 6-phosphate [27]. Accurate substrate concentrations were determined by the measurement of absorbance changes that corresponded to the total consumption of substrates in triplicate. The reaction components BTP buffer, MnSO_4 , PEP, E4P and inhibitor were incubated for two minutes at 25 °C to ensure equilibration before the addition of 2 μL of 0.9 mg mL^{-1} *Nme*DAH7PS. Final assay conditions were 100 μM MnSO_4 , 115 μM E4P, 19.9–79.6 μM PEP, and variable concentrations of the inhibitors (18.9–151.2 μM vinyl phosphonate **6** inhibitor, 202–1616 μM (*R*)-phospholactate **7** and 268–2144 μM (*S*)-phospholactate **8**). BTP buffer was added to each cuvette to bring the final volume to 1 mL. The values of K_i and K_m were determined by fitting all the initial-rate data points using non-linear regression to the Michaelis–Menten equation modified for the presence of a competitive inhibitor (Eq. (1) below) using Graft (Erithicus software).

$$v = \frac{V_{\max}[\text{PEP}]}{K_m(1 + [\text{I}]/K_i) + [\text{PEP}]} \quad (1)$$

2.3. Co-crystallisation of inhibitors with *Nme*DAH7PS

*Nme*DAH7PS was overexpressed and purified as previously described [17]. Co-crystallisation of the protein and inhibitor was

achieved by preparing a solution containing approximately 5 mM inhibitor dissolved in 10 mM BTP (pH 7.3). 400 μL of this solution was added to the stock solution containing 50 μL of 10 mg mL^{-1} enzyme and was concentrated to 50 μL using a 10 kDa molecular weight cut-off membrane (Vivaspin). The resulting solution was diluted again with 400 μL of inhibitor solution and concentrated by centrifugation. This process was repeated four times. The resulting protein solution was concentrated to approximately 10 mg mL^{-1} . 1 μL of the buffer-exchanged enzyme solution (9–11 mg mL^{-1}) was mixed with 1 μL of crystallisation buffer containing 0.1 M Tris HCl (pH 7.3), 0.2 M trimethyl-amino-*N*-oxide (TMAO), 0.4 mM MnSO_4 and 15–20% (w/v) PEG 2000MME. Crystals were grown by hanging-drop vapour diffusion over 500 μL of crystallisation buffer and the crystallisation trays were incubated at 20 °C. Crystals began to form in 24 h and were fully formed within three days. Crystals were flash frozen using liquid nitrogen in a cryoprotectant solution containing reservoir solution and 20% (v/v) PEG400.

2.4. Crystallography and structure determination

X-ray diffraction datasets were collected at the Australian synchrotron using the MX1 and MX2 beamlines [28]. The datasets were integrated and processed using XDS and aimless (CCP4 program suite) [29,30]. The appropriate cut-off resolution was determined via $\text{CC}^{1/2} \geq 0.5$ while ensuring the data set was complete in the highest resolution shell [31]. For the co-crystal structures with the vinyl phosphonate and (*S*)-phospholactate ligands, the space group ($P2_12_1$) and unit cell parameters were the same as those previously identified for *Nme*DAH7PS (PDB code 4HSN [17]). To minimise bias, all ligands and waters were removed from the search model (PDB code 4HSN) before molecular replacement (Phaser MR (CCP4) [32]) was carried out. When co-crystallised with (*R*)-phospholactate, *Nme*DAH7PS crystallised, non-isomorphously, in the orthorhombic space group, $P2_12_12_1$. Although structure solution and refinement proceeded normally, the data collected were affected by anisotropy. Refmac5 was used to generate the electron density maps for all three structures and these were manually analysed to develop the structural model by means of COOT [33–35]. The quality of the model was optimised by consecutive model building in COOT and refinement with Refmac5. Water molecules were added manually via interpretation of the $(2|F_o| - |F_c|)$ and $(|F_o| - |F_c|)$ maps, with the requirement that putative water molecules had at least one hydrogen-bonding partner. In all structures, no electron density for the 14 amino acids at the N-terminus of each *Nme*DAH7PS chain could be found, which is attributed to these residues being part of a conformationally highly flexible allosteric binding loop [17]. Residues Met1–Asp9 were also absent from the model (PDB code 4HSN) used for molecular replacement. Molprobtity [36] and the validation tools of COOT were used to assess structure quality during refinement cycles and before deposition [36]. After refinement of all protein and non-active-site water molecules had been completed, electron density that could be interpreted as the respective inhibitors could be observed in the active site. CIF files for all three inhibitors were built using the Dundee PRODRG2 server [37]. The inhibitors were positioned manually into this electron density using COOT and then refined. In all three structures, model elaboration and refinement continued until no further improvement in R_{free} could be gained and for final refinements NCS restraints were dropped.

The (*R*)-phospholactate **7** structure crystallised in the orthorhombic space group $P2_12_12_1$ as confirmed by the presence of systematic absences for this space group, and the subsequent successful structure solution and refinement. The data are noticeably anisotropic such that diffraction in the b^* direction is relatively very much weaker than in the other directions, especially at higher

resolution; this is the cause of the high overall R_{merge} (0.298). The low Wilson B value of 19.65 \AA^2 vis-à-vis resolution of this dataset is biased by strong diffraction in the other two directions; it is not the result of overlooked twinning, for which no evidence could be found from intensity statistics nor from metrical relationships among unit cell parameters. Notwithstanding anisotropy in the diffraction data, electron-density maps were of noticeably higher quality upon inclusion of the high-resolution data. In this (and the other two structures) the refined average B value was similar to the respective Wilson B value. The final value for R_{free} (0.227) and the small difference between R_{free} and R_{work} (0.026) indicate that this structure (and also the other two structures, which had similarly favourable values) had not been over-refined.

Distances given in the structural analysis of inhibitor binding are defined as a range in \AA across all subunits of the tetramer, to ensure consistency during comparison. Only distance differences that remain consistent throughout all subunits during comparison of respective structures are included.

3. Results and discussion

3.1. NmeDAH7PS is inhibited by PEP analogues

Previous studies have shown that both *Eco*DAH7PS and *Mtu*DAH7PS were inhibited by compounds that possess either a planar trigonal or a tetrahedral geometry at C2 [3,22,23]. Both phospholactate stereoisomers **7** and **8** and the vinyl phosphonate **6** were synthesised and tested as inhibitors of *Nme*DAH7PS. All three compounds were found to inhibit *Nme*DAH7PS competitively with respect to substrate PEP. The most potent inhibitor was the vinyl phosphonate **6**, with an observed K_i value of $3.9 \pm 0.4 \text{ }\mu\text{M}$. This value is significantly lower than the measured K_m for PEP ($12 \text{ }\mu\text{M}$). While both enantiomers of the phospholactate were also inhibitory, inhibition by the (*R*)-phospholactate **7** was 3.5 times greater than that observed for the (*S*)-phospholactate **8** (Table 2).

The order of inhibitory potency observed for these compounds with *Nme*DAH7PS parallels the observations made for the type I α *Eco*DAH7PS. For *Eco*DAH7PS, the (*R*)-phospholactate **7** was shown to be more than 10-fold more potent than the (*S*)-stereoisomer [23]. The *Mtu*DAH7PS enzyme also demonstrated this same stereochemical preference for the configuration at C2 when tested with the extended bisphosphate inhibitors **9** and **10** [3,24]. The most potent of these bisphosphate inhibitors was the (*R*)-bisphosphate **9**, which exhibited a K_i value of $0.36 \pm 0.05 \text{ }\mu\text{M}$ (in comparison to the (*S*)-bisphosphate **10** with a K_i of $0.6 \pm 0.1 \text{ }\mu\text{M}$) [3]. Thus, stereochemical influences on inhibitor-binding affinity appear to be intrinsic to the active sites of DAH7PS and are independent of the class of DAH7PS and the species from which the enzyme is derived.

The increase in potency upon introduction of a phosphonate with a planar geometry at C2, observed for vinyl phosphonate **6**, is consistent with what has been reported previously for *Eco*DAH7PS [23]. It should be noted that all these inhibitors are particularly potent with respect to their size, showing very high ligand efficiencies (ligand efficiency (LE) = $\Delta G/N$; where $\Delta G = -RT \ln K_i$ and N = number of non-hydrogen atoms per ligand) [38,39]. When comparing the relative ligand efficiencies of the vinyl phosphonate measured here for *Nme*DAH7PS, and the extended (*R*)-bisphosphate **9** (as an inhibitor of *Mtu*DAH7PS), it is evident that the vinyl phosphonate **6** is 1.6-fold more efficient than the longer inhibitor. The (*R*)-bisphosphate **9** is the most potent inhibitor reported for any DAH7PS enzyme to date [3].

3.2. Structural analysis of inhibitor binding

Structures of *Nme*DAH7PS co-crystallised with each of the inhibitors were determined by X-ray diffraction. The three

structures containing the ligands vinyl phosphonate **6**, (*R*)-phospholactate **7** and (*S*)-phospholactate **8** were refined to resolutions of 1.76 \AA , 2.17 \AA and 2.35 \AA respectively (Table 1). The vinyl phosphonate and (*S*)-phospholactate-bound proteins crystallised in the same space group (monoclinic $P12_11$) as the wild-type protein, whereas the (*R*)-phospholactate-bound enzyme crystallised in the orthorhombic space group $P2_12_12_1$. The asymmetric unit for all three inhibitor-bound structures contained a homotetramer.

Continuous electron density for the three ligands was observed in all active sites after complete refinement of the protein and non-active-site water molecules (Fig. 2). Judging from B values of ligands and ligand-binding side chains, the ligands are present in full, or close to full, occupancy. The binding of inhibitors does not affect the secondary or tertiary structure of the enzyme. Individual subunits within a tetramer superimpose on each other with a root-means-square displacement (RMSD) of between 0.05 and 0.09 \AA , whereas superposition of subunits from different tetramers superimpose with RMSD values in the range 0.10 to 0.18 \AA .

The inhibitors show similar placement within the active site and binding modes to that observed for the natural substrate PEP **1** (Fig. S4, Supplementary material). The side chains of residues Lys188, Arg167 and Arg236 and the main-chain peptide N of Ala166 that interact with the phosphate moiety of PEP form similar interactions with the phosphate or phosphonate functionalities of the three ligands, consistent with this portion of each inhibitor being able to mimic the PEP binding characteristics well. Mn^{2+} is found in the metal-binding site of all the structures in full occupancy. As well as coordinating to the Mn^{2+} in the active site, the carboxylate group of each ligand forms salt bridges with the side chain of Arg94 and with the side chain of Lys99 of the conserved LysProArgThr motif, which extends into the E4P binding site. In the structure of the PEP-bound enzyme, Mn^{2+} also coordinates the PEP carboxylate functionality and a water molecule. The lack of this coordinating water molecule in any of the inhibitor-bound structures is associated with a closer positioning of the carboxylate group of the respective PEP-mimic to the metal ion (Fig. S2).

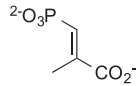
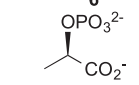
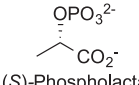
There are five waters in the active site of each subunit occupying similar positions in the vicinity of both the vinyl phosphonate **6** and (*R*)-phospholactate **7** inhibitors (labelled WAT1–5, Fig. 2). WAT1 is found in a position corresponding to the *re* face of PEP and establishes hydrogen bonds with the bridging oxygen of the phosphate group and with a terminal oxygen of the phosphate or phosphonate functionalities. Additionally, WAT1 hydrogen-bonds to WAT2 and Glu145. WAT2 also forms hydrogen-bonding interactions with Lys188 and Tyr96. WAT3 is also hydrogen-bonded to the phosphate or phosphonate moieties and interacts with the backbone amino group and the η^1 nitrogen of Arg167. WAT4 forms hydrogen-bonding interactions with both η^1 and η^2 of Arg167 and to an oxygen of the phosphate or phosphonate functionalities. WAT5 makes no direct interactions with the inhibitors, but provides a hydrogen-bonding bridge between Glu145 and Lys99. WAT1, WAT2, WAT3 and WAT5 are also found occupying similar positions in the (*S*)-phospholactate **8** inhibitor-bound structure. No evidence for a WAT4 was observed for this structure, although it is noted that this structure has the lowest resolution of this set. All five of these water molecules were also present in the PEP-bound structure, although WAT4 is only modelled into chain A of this structure [17]. In addition, as noted earlier, a Mn^{2+} -coordinated water is observed in the PEP-bound structure.

Tertiary structures, as noted above, are unaffected by inhibitor binding and the tetrameric quaternary structures of *Nme*DAH7PS bound with (*S*)-phospholactate and vinyl phosphonate are identical to that of the isomorphous PEP-bound parent structure (PDB code 4HSN) (RMSDs for superposition onto 4HSN of 0.17 and 0.23 \AA for 1328 and 1327 C α atoms, respectively). However, there are small but significant changes in the arrangement of subunits

Table 1
Data collection and refinement.

	<i>NmeDAH7PS</i> complex		
	Vinyl phosphonate 6	(<i>R</i>)-phospholactate 7	(<i>S</i>)-phospholactate 8
Data Collection			
Crystal system; space group	Monoclinic, <i>P</i> 12 ₁ 1	Orthorhombic, <i>P</i> 2 ₁ 2 ₁ 2 ₁	Monoclinic, <i>P</i> 12 ₁ 1
Unit cell parameters			
<i>a</i> , <i>b</i> , <i>c</i> (Å)	73.49, 136.50, 76.16	79.44, 133.7, 147.2	73.42, 137, 76.48
α , β , γ (°)	90, 96.41, 90	90, 90, 90	90, 96.48, 90
Resolution range (Å)	46.82–1.76 (1.79–1.76)	48.31–2.17 (2.21–2.17)	46.88–2.34 (2.40–2.34)
Measurements	1,113,629	617,846	242,429
Unique reflections	147,006	83,610	63,250
Redundancy	7.6	7.4	3.8
Completeness (%)	99.8 (99.2)	99.9 (98.7)	99.9 (99.8)
<i>I</i> / σ (<i>I</i>)	16.9 (1.9)	6.5 (1.2)	8.0 (1.1)
<i>R</i> _{merge}	0.070	0.298	0.148
CC _{1/2}	0.88	0.52	0.50
Wilson <i>B</i> value (Å) ²	24.52	19.65	30.63
Matthews coefficient	2.50	2.57	2.51
Refinement			
<i>R</i> _{work}	0.1918	0.2007	0.2040
<i>R</i> _{free}	0.2144	0.2267	0.2304
Chain length	351	351	351
Observed number of residues	333 (Chain C & D) 332 (Chain A & B)	333 (Chain A), 332 (Chain B, C & D)	333 (Chain A & B), 334 (Chain C), 332 (Chain D)
Water molecules	779	634	263
Other	4	8	8
Ligand	4	4	4
Mean <i>B</i> (Å)²			
Protein	32.87	24.90	38.37
Water	34.50	24.42	30.42
Other	23.66	33.12	57.93
Ligand	24.35	22.54	40.23
<i>R.m.s.d</i> from target values			
Bond lengths (Å)	0.0104	0.0106	0.0117
Bond angles	1.3822	1.3951	1.4594
Dihedral angles	0.0800	0.0745	0.0761
Ramachandran			
Preferred (%)	97.71	97.54	98.36
Allowed (%)	1.68	1.84	1.22
Outliers (%)	0.61	0.61	0.61
PDB Entry	4UMA	4UMB	4UMC

Table 2
Inhibition constants of compounds tested against *NmeDAH7PS*.

Inhibitor	<i>K_i</i> (μM) ^a
 Vinyl phosphonate 6	3.9 ± 0.4
 (<i>R</i>)-Phospholactate 7	99 ± 16
 (<i>S</i>)-Phospholactate 8	360 ± 30

^a Assay conditions used were 100 μM MnSO₄, 115 μM E4P, 19.9–79.6 μM PEP, 18.9–151.2 μM vinyl phosphonate inhibitor **6**, 202–1616 μM (*R*)-phospholactate **7**, and 268–2144 μM (*S*)-phospholactate **8**. A graphical representation of the data is provided in the supplementary material (Fig. S1 and Table S1).

for the non-isomorphous (*R*)-phospholactate structure relative to the PEP-bound parent (RMSD of 0.60 Å for superposition of 1325 Cα atoms). The tetramer is made up of two dimers, one comprising an extensive interface with mutual proximity of the E4P binding loops (β2α2), often referred to as the tight dimer interface, the

other dimer, often referred to as the loose dimer interface, being formed largely by antiparallel association of helix α0. The quaternary structural changes are concentrated at the weak dimer interface, the tight dimers superimposing on PEP-bound enzyme with RMSDs in the range 0.13–0.27 Å. Thus, these differences between the (*R*)-phospholactate-bound structure and the PEP-, (*S*)-phospholactate- and vinyl phosphonate-bound structures can be attributed to crystal packing effects (sampling different conformations of the ensemble of quaternary structures freely sampled in solution).

3.3. Small differences in inhibitor binding modes are observed

While the binding modes of the two phospholactate enantiomers are very similar, a comparison of the (*R*)- and (*S*)-phospholactate inhibitor-bound structures and the different way in which the two stereoisomers can be accommodated in the active site highlights some small differences in the relative positions of the key functional groups which may account for their inhibitory differences (Fig. 3). These differences are shared when any subunit of one tetramer is compared to any subunit of another tetramer, consistent with the very high similarity of all individual subunits described above. This allows small differences of marginal significance in a single pairwise comparison to become highly significant when all subunits are compared. The phosphate groups of the two molecules are similarly positioned and a slight displacement of the carboxylate functionality of (*R*)-phospholactate away from Lys99 towards Arg94 is observed. WAT1 is found in closer proximity to

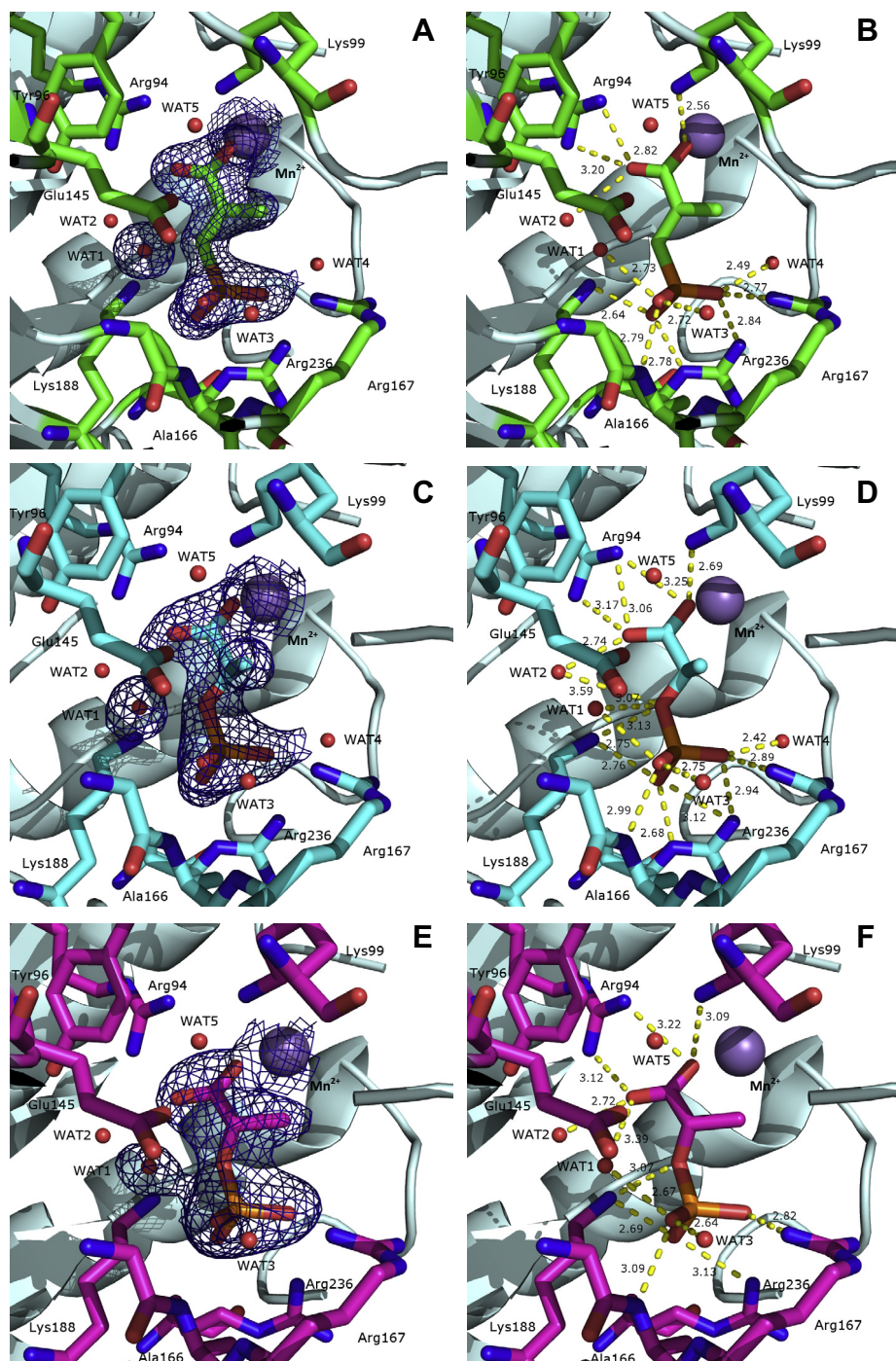


Fig. 2. Structure of *NmeDAH7PS* in complex with inhibitors. Panels A and B: vinyl phosphonate **6** bound structure (chain A). Panels C and D: (*R*)-phospholactate **7** bound structure (chain A). Panels E and F: (*S*)-phospholactate **8** bound structure (chain A). Panels B, D and F show interatomic distances (in Å). Panels A, C and E display the $[2Fo - Fc]$ map to indicate the observed electron density for the bound ligand and WAT1 contoured at 1σ . The interatomic distances for each chain and the omit maps are provided in the supplementary material (Figs. S3–S7). Mn^{2+} is shown as a purple sphere in all panels.

C2 of the (*S*)-phospholactate than the (*R*)-phospholactate (by 0.2–0.7 Å by comparison across all chains), bringing this separation to less than van der Waals distance. This is likely to be a direct result of the configurational difference between the two phospholactate inhibitors. The stereochemical difference will necessarily result in the C2 hydrogen of the inhibitor pointing directly towards WAT1 when (*S*)-phospholactate is bound, whereas for the (*R*)-enantiomer, this hydrogen will be positioned away from WAT1 (Fig. 4). In addition, the positioning of the (*R*)-phospholactate allows for more optimal hydrogen-bonding interactions to WAT1,

as can be seen when the angles (C2 phospholactate-bridging phosphate oxygen-WAT1) are compared between the (*R*)- and (*S*)-phospholactate inhibitor-bound structures: for (*S*)-phospholactate, this angle is close to 90° , leading to poor hydrogen-bonding interactions when the direction of the lone pair electrons of the bridging oxygen is considered. In contrast, the angle (C2 phospholactate-bridging phosphate oxygen-WAT1) is close to 109° in the (*R*)-phospholactate bound structure, which leads to a close to optimal angular geometry for a hydrogen bond between WAT1 and the bridging phosphate oxygen in the (*R*)-phospholactate ligand. In

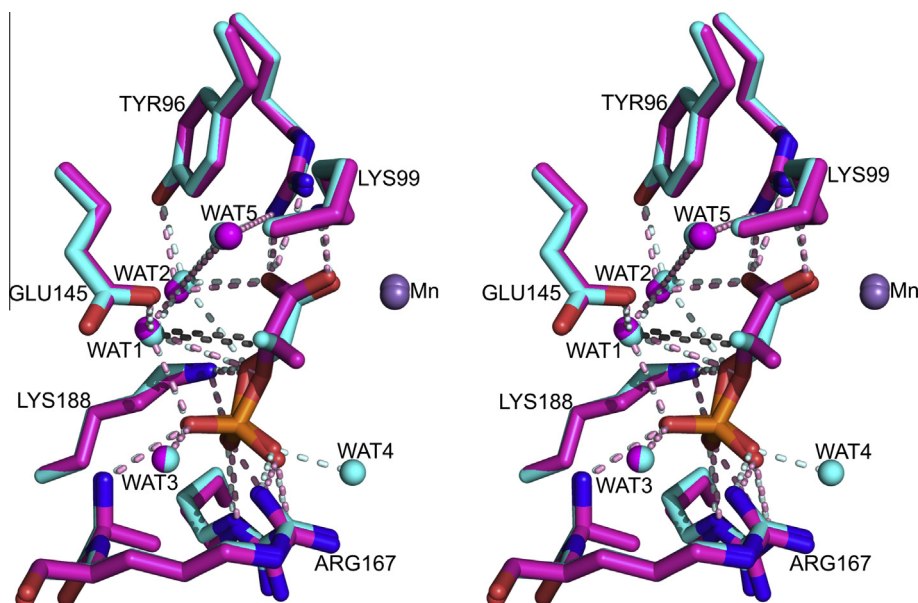


Fig. 3. Comparison of binding modes of (*R*)- and (*S*)-phospholactate in stereo view. (*R*)-Phospholactate is shown in cyan and (*S*)-phospholactate is shown in magenta. Interatomic distances are shown as pale cyan dashes for the (*R*)-phospholactate interactions and pink dashes for the (*S*)-phospholactate interactions. Distances between WAT1 and C2 of the ligand are 3.8 Å for (*R*)-phospholactate and 3.3 Å for the (*S*)-phospholactate (shown as grey dashes). Mn^{2+} is shown as a purple sphere. The carboxylate and phosphate moieties of both inhibitors are in very similar positions, which correspond well to the placement of these moieties when the substrate PEP is bound; the positions of ligand-binding side chains do not change significantly on ligand binding. However, a slight displacement of the bridging phosphate oxygen is apparent, along with the methyl substituent, which results in an altered hydrogen-bonding geometry between WAT1 and the bridging phosphate oxygen.

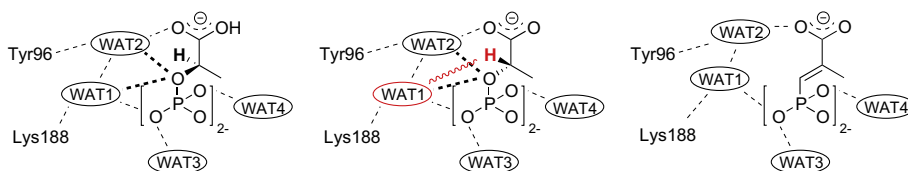


Fig. 4. Schematic representation of subtle differences in the water-mediated hydrogen-bonding network in the inhibitor bound crystal structures. For (*R*)-phospholactate (left), the C2–hydrogen (bold) points away from WAT1. For (*S*)-phospholactate (centre), the C2–hydrogen (bold and red) points towards WAT1, potentially resulting in steric hindrance (indicated by red wavy line). Both phospholactate enantiomers establish hydrogen-bonding interactions with WAT1 and WAT2 through the bridging phosphate oxygen (dotted lines). These interactions are not observed in the binding mode of *E*-vinyl phosphonate (right), which has a bridging methylene group instead of an oxygen.

summary, these small differences in the co-crystal structures of *NmeDAH7PS* in complex with the two enantiomers of phospholactate, improved accommodation of WAT1 and a more optimal hydrogen-bonding network between the inhibitor and the active-site waters may serve to explain the difference in potency of the enantiomeric phospholactates. Our study reveals that the small differences in inhibitory potency correlate with subtly different binding modes of the inhibitors as could have been predicted; however, the precise structural information obtained here on the enzyme–inhibitor co-crystal structures will help inform future inhibitor design.

The increased inhibitor potency observed for the vinyl phosphonate **6** over the (*R*)-phospholactate **7** suggests that the active site is better prepared to accommodate a planar rather than tetrahedral intermediate. This occurs despite the lack of a hydrogen bond acceptor in the vinyl phosphonate, which results in one less hydrogen bond being established between the vinyl phosphonate and WAT1. Although a similar binding mode is adopted by both inhibitors and the distances between the phosphonate or phosphate moieties of these inhibitors and the residues with which they interact are very similar, there are small structural differences that may be relevant to this change in functionality and potency. The bridging oxygen of the phosphate in the (*R*)-phospholactate is 0.1–0.4 Å closer to Lys188 than the bridging carbon of the phosphonate functionality in the vinyl phosphonate. A small relative

displacement (0.1–0.3 Å) of the carboxylate functionality of the vinyl phosphonate towards to the amino group of Lys99 is also apparent. This shift in the binding mode of the vinyl phosphonate towards Lys99 compromises the interaction between the carboxylate functionality and WAT2, which are further apart (0.2–0.5 Å) in the vinyl phosphonate bound structure. However, the planar and more compact geometry of the vinyl phosphonate compared to (*R*)-phospholactate enables closer proximity and thus a stronger Coulomb interaction to develop between the negative charge of the vinyl phosphonate carboxylate and the potentially positively charged Lys99 amino group. Another key factor in the stronger binding of the vinyl phosphonate compared to the phospholactate moieties is that the rotational/torsional degrees of freedom around the C1–C2 and the C2–C3 bond are surrendered upon binding to the enzyme for the phospholactate species, in contrast to minimal loss of such degrees of freedom when the more rigid vinyl phosphonate binds. This can be estimated to contribute a free-energy stabilisation as $2R\ln 3$ (allowing three torsional conformations), that is $\sim 5.4 \text{ kJ mol}^{-1}$ at 25 °C, or a factor of ~ 9 in terms of equilibrium constant, a number remarkably similar to the relative affinities of binding of the vinyl phosphonate compared to the more easily accommodated (*R*)-enantiomer of the phospholactate species.

The accommodation of WAT1 appears to be an important feature of all the inhibitor–*NmeDAH7PS* structures. The distance

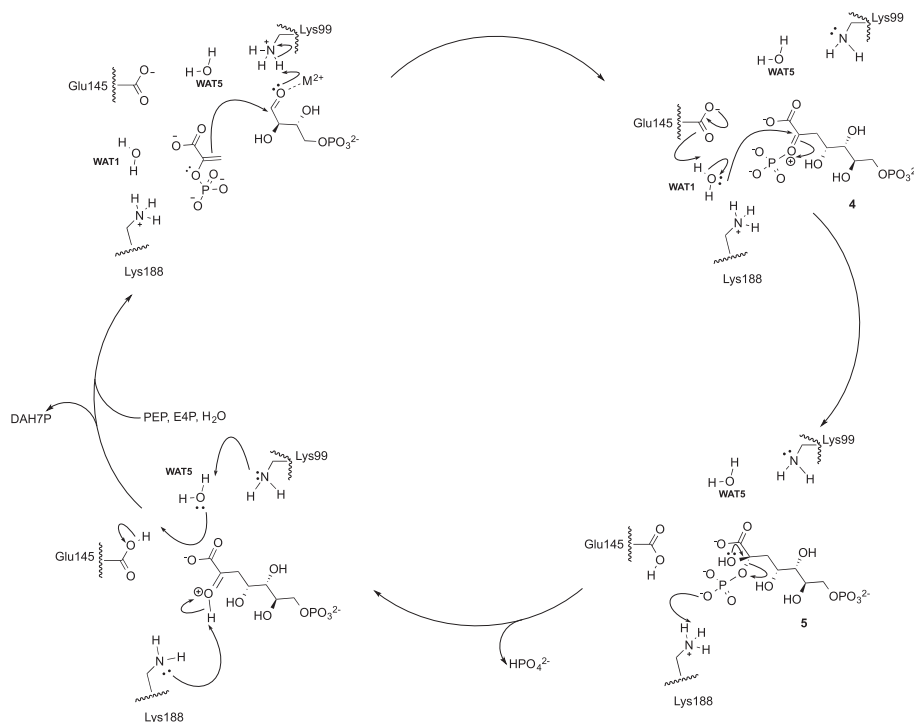


Fig. 5. Proposed mechanism of catalysis of *NmeDAH7PS* showing key nucleophilic role for active site WAT1.

from WAT1 to C2 of the vinyl phosphonate is (0.1–0.3 Å) closer than is that observed for the (*R*)-phospholactate-bound structure. This difference appears to be a direct result of the planarity resulting from the double bond of the vinyl phosphonate concomitant with the fixing of the carboxylate and phosphate moieties into their binding pockets. Taken together with the inhibition constants, this analysis suggests that the geometry of the *NmeDAH7PS* active site is better optimised to accommodate a planar reaction intermediate or mimic (vinyl phosphonate) thereof, in combination with the nucleophilic WAT1. The loss of a hydrogen bonding contact when moving from the phospholactates to vinyl phosphonate appears to be outweighed by WAT1 being able to be accommodated at a slightly better van der Waals separation than the (*R*)-phospholactate, which at 3.8–3.9 Å is slightly longer (and (*S*)-phospholactate which is noticeably shorter) than ideal van der Waals contact, even after allowing for different hybridisation of carbon atom C2.

3.4. Implications for the mechanism of the DAH7PS-catalysed reaction

The cleavage of the C–O bond to release phosphate in the reaction catalysed by DAH7PS demands that water acts as a co-substrate in the reaction (Fig. 1). Coordination of the aldehydic group of E4P to the divalent active site metal ion both assists in presenting the *re* face of the aldehyde group to the *si* face of PEP and thus pre-organises the substrates for nucleophilic attack by PEP through its C3. It is likely that an oxocarbenium-like transition state or transient intermediate is then quenched by water to generate a tetrahedral intermediate. The direction of attack of this water determines the stereochemistry of this intermediate. From the structural information gathered in these ligand-bound structures, it is evident that the most likely candidate for the nucleophilic water is indeed WAT1 based on its proximity to C2 of PEP, supporting the attack by water on the *re* face of PEP, overall *anti* addition across the PEP-double bond, and the generation of a transient stereogenic centre in the intermediate with an (*S*) absolute configuration. In support of this, water has been observed to

occupy similar positions in the DAH7PS structures from *Saccharomyces cerevisiae*, *E. coli*, *M. tuberculosis* and *Thermotoga maritima* [3,6,13,14].

The preference for the binding of the (*R*)-phospholactate over the (*S*)-phospholactate and the structural observations from these ligand-bound structures are also consistent with *re* face water attack and the generation of (*S*)-configuration at C2 of the tetrahedral intermediate. A greater than 3-fold difference in potency between the (*R*)- and (*S*)-phospholactate inhibitors results from change in absolute configuration at C2. Although an (*S*)-configuration of the phosphohemiketal tetrahedral intermediate **5** will arise from *re* face water attack, the closer placement of C2 of the (*S*)-phospholactate and the corresponding requirement to accommodate a hydrogen on C2 of the phospholactate likely hinders co-occupation of the active site with this water molecule, accounting for the reduced potency observed for the (*S*)-phospholactate. Conversely, (*R*)-phospholactate, with the hydrogen at C2 pointing away from the active site water more readily accommodates WAT1. A similar stereochemical preference was also observed for the extended (*R*)- and (*S*)-bisphosphate inhibitors **9** and **10** for *MtuDAH7PS*. While the preference for the (*R*)-configuration was only twofold, the differences in potency were also attributed to better accommodation of a water molecule in an equivalent position to WAT1 from this study [3].

The planar geometry of the vinyl phosphonate is accompanied by a significant increase in potency over either of the phospholactate stereoisomers. The double bond introduced at C2 is able to mimic the prochirality seen in the oxocarbenium ion intermediate, which further suggests that the planar ligand geometry is best suited to accommodate the binding of the nucleophilic water molecule (WAT1). Therefore, among the three ligands examined in this study, the ability for the inhibitor to adequately accommodate WAT1 upon binding and the lessened changes in conformational flexibility on binding with respect to the free ligand are the defining criteria for inhibitor potency. From our structural analysis, we propose that (*R*)-phospholactate is a stronger inhibitor than (*S*)-phospholactate, in part due to improved hydrogen-bond

geometry between WAT1 and the bridging phosphate oxygen in (R)-phospholactate and in part due to lesser stereochemical clash of WAT1 with C2. We further suggest that the highest potency of the planar vinyl phosphonate inhibitor is due in part to lowered loss of conformational flexibility of this more rigid ligand on binding to the enzyme and in part on WAT1 being placed in ideal proximity to C2 of the ligand. This position may most resemble that which WAT1 would assume during the course of regular enzymatic turnover, acting as the nucleophilic water which attacks C2 of the oxocarbenium ion **4** (Fig. 1).

With the identification of the nucleophilic water, the details of the *Nme*DAH7PS-catalysed reaction mechanism can be elucidated from the kinetic and structural data presented here in combination with previous mechanistic and structural studies on DAH7PS from other sources (Fig. 5) [3,10]. Nucleophilic attack of PEP at the E4P aldehyde moiety is facilitated by activation of the carbonyl moiety by coordination to the active-site metal ion and subsequent protonation of the nascent alkoxo group by Lys99. The transient oxocarbenium ion species **4** is then rapidly attacked by WAT1, which is deprotonated by Glu145, resulting in the formation of the tetrahedral intermediate **5**. This nucleophilic water is held in position on the *re* face of PEP by hydrogen bonds to Glu145 and WAT2. Glu145 is conserved in both sequence and structure in all known DAH7PS enzymes [3,13]. Lys99 residue is protonated via an active site water molecule by Glu145. Lys188, which is positioned within proximity for hydrogen bonding interactions with the phosphate of PEP, is predicted to aid in the elimination of phosphate from the tetrahedral intermediate **5** via protonation of the leaving group. Elimination of phosphate results in the linear DAH7P product, which is protonated at the 2-keto moiety. Deprotonation of this species by Lys188 subsequently results in the formation of the product, DAH7P, which is in equilibrium with its pyranose form **3**, and restores the enzyme for a subsequent catalytic cycle (Fig. 5).

4. Conclusion

Three PEP mimics were found to be inhibitors of *Nme*DAH7PS and to occupy the PEP binding pocket of the active site of this enzyme. Analysis of the first co-crystal structures of these small but highly atom-efficient inhibitors with their target enzyme highlight the importance of the accommodation of the nucleophilic water molecule in the active site for potent inhibition. From our studies we conclude that planar rather than tetrahedral PEP-mimics are more promising candidates for inhibition of *Nme*DAH7PS, and the ability of inhibitors to accommodate the key nucleophilic water molecule needs to be considered in future inhibitor design. Extension of a planar ligand based on the rigid vinyl phosphonate scaffold facilitated by the first structural information on enzyme-inhibitor complexes presented here would likely be a highly potent inhibitor of *Nme*DAH7PS.

Acknowledgments

This research was undertaken on the MX1 and MX2 beamlines at the Australian Synchrotron, Victoria, Australia. Funding is gratefully acknowledged for these studies from the New Zealand Marsden Fund (UOC1105). S.R. is grateful for financial support from a University of Canterbury Doctoral Scholarship and a New Zealand International Doctoral Research Scholarship.

Appendix A. Supplementary material

Supplementary data associated with this article can be found, in the online version, at <http://dx.doi.org/10.1016/j.bioorg.2014.08.003>.

References

- [1] R. Bentley, Crit. Rev. Biochem. Mol. Biol. 25 (1990) 307–384.
- [2] H. Maeda, N. Dudareva, Annu. Rev. Plant Biol. 63 (2012) 73–105.
- [3] S. Reichau, W. Jiao, S.R. Walker, R.D. Hutton, E.N. Baker, E.J. Parker, J. Biol. Chem. 286 (2011) 16197–16207.
- [4] V.F.V. Prazeres, L. Tizon, J.M. Otero, P. Guardado-Calvo, A.L. Llamas-Saiz, M.J. van Raaij, L. Castedo, H. Lamb, A.R. Hawkins, C. Gonzalez-Bello, J. Med. Chem. 53 (2010) 191–200.
- [5] J.R. Coggins, C. Abell, L.B. Evans, M. Frederickson, D.A. Robinson, A.W. Roszak, A.P. Laphorn, Biochem. Soc. Trans. 31 (2003) 548–552.
- [6] I.A. Shumilin, R. Bauerle, J. Wu, R.W. Woodard, R.H. Kretsinger, J. Mol. Biol. 341 (2004) 455–466.
- [7] H.G. Floss, D.K. Onderka, M. Carroll, J. Biol. Chem. 247 (1972) 736–744.
- [8] A.B. DeLeo, D.B. Sprinson, Biochem. Biophys. Res. Commun. 32 (1968) 873–877.
- [9] D.K. Onderka, H.G. Floss, J. Am. Chem. Soc. 91 (1969) 5894–5896.
- [10] M. Ahn, A.L. Pietersma, L.R. Schofield, E.J. Parker, Org. Biomol. Chem. 3 (2005) 4046–4049.
- [11] R.M. Williamson, A.L. Pietersma, G.B. Jameson, E.J. Parker, Bioorg. Med. Chem. Lett. 15 (2005) 2339–2342.
- [12] S.R. Walker, E.J. Parker, Bioorg. Med. Chem. Lett. 16 (2006) 2951–2954.
- [13] V. König, A. Pfeil, G.H. Braus, T.R. Schneider, J. Mol. Biol. 337 (2004) 675–690.
- [14] I.A. Shumilin, R.H. Kretsinger, R.H. Bauerle, Structure (London) 7 (1999) 865–875.
- [15] L.R. Schofield, B.F. Anderson, M.L. Patchett, G.E. Norris, G.B. Jameson, E.J. Parker, Biochemistry 44 (2005) 11950–11962.
- [16] C.J. Webby, H.M. Baker, J.S. Lott, E.N. Baker, E.J. Parker, J. Mol. Biol. 354 (2005) 927–939.
- [17] P.J. Cross, A.L. Pietersma, T.M. Allison, F.C. Cochrane, E.J. Parker, Protein Sci. 22 (2013) 1087–1099.
- [18] L. Zhou, J. Wu, V. Janakiraman, I.A. Shumilin, R. Bauerle, R.H. Kretsinger, R.W. Woodard, Bioorg. Chem. 40 (2012) 79–86.
- [19] S.H. Light, A.S. Halavaty, G. Minasov, L. Shuvalova, W.F. Anderson, Protein Sci. 21 (2012) 887–895.
- [20] R.A. Jensen, G. Xie, D.H. Calhoun, C.A. Bonner, J. Mol. Evol. 54 (2002) 416–423.
- [21] C.J. Webby, W. Jiao, R.D. Hutton, N.J. Blackmore, H.M. Baker, E.N. Baker, G.B. Jameson, E.J. Parker, J. Biol. Chem. 285 (2010) 30567–30576.
- [22] S.R. Walker, W. Jiao, E.J. Parker, Bioorg. Med. Chem. Lett. 21 (2011) 5092–5097.
- [23] S.R. Walker, H. Cumming, E.J. Parker, Org. Biomol. Chem. 7 (2009) 3031–3035.
- [24] S. Reichau, E.J. Parker, RSC Adv. 3 (2013) 3209–3212.
- [25] N.E. Rosenstein, B.A. Perkins, D.S. Stephens, T. Popovic, J.M. Hughes, New England J. Med. 344 (2001) 1378–1388.
- [26] P.A. Lanzetta, L.J. Alvarez, P.S. Reinach, O.A. Candia, Anal. Biochem. 100 (1979) 95–97.
- [27] C.E. Ballou, H.O.L. Fischer, D. MacDonald, J. Am. Chem. Soc. 77 (1955) 5967–5970.
- [28] T.M. McPhillips, S.E. McPhillips, H.J. Chiu, A.E. Cohen, A.M. Deacon, P.J. Ellis, E. Garman, A. Gonzalez, N.K. Sauter, R.P. Phizackerley, S.M. Soltis, P. Kuhn, J. Synchrotron Rad. 9 (2002) 401–406.
- [29] P.R. Evans, Acta Crystallogr. D Biol. Crystallogr. 67 (2011) 282–292.
- [30] P. Evans, Acta Crystallogr. D Biol. Crystallogr. D62 (2006) 72–82.
- [31] P.A. Karplus, K. Diederichs, Science 336 (2012) 1030–1033.
- [32] A.J. McCoy, R.W. Grosse-Kunstleve, P.D. Adams, M.D. Winn, L.C. Storoni, R.J. Read, J. Appl. Crystallogr. 40 (2007) 658–674.
- [33] G.N. Murshudov, P. Skubak, A.A. Lebedev, N.S. Pannu, R.A. Steiner, R.A. Nicholls, M.D. Winn, F. Long, A.A. Vagin, Acta Crystallogr. D Biol. Crystallogr. 67 (2011) 355–367.
- [34] G.N. Murshudov, A.A. Vagin, E.J. Dodson, Acta Crystallogr. Sect. D: Biol. Cryst. 53 (1997) 240–255.
- [35] P. Emsley, B. Lohkamp, W.G. Scott, K. Cowtan, Acta Crystallogr. D Biol. Crystallogr. 66 (2010) 486–501.
- [36] V.B. Chen, W.B. Arendall III, J.J. Headd, D.A. Keedy, R.M. Immormino, G.J. Kapral, L.W. Murray, J.S. Richardson, D.C. Richardson, Acta Crystallogr. D Biol. Crystallogr. D66 (2010) 12–21.
- [37] A.W. Schüttelkopf, D.M.F. van Aalten, Acta Crystallogr. D Biol. Crystallogr. 60 (2004) 1355–1363.
- [38] I.D. Kuntz, K. Chen, K.A. Sharp, P.A. Kollman, Proc. Natl. Acad. Sci. USA 96 (1999) 9997–10002.
- [39] S.D. Bembenek, B.A. Tounge, C.H. Reynolds, Drug Discovery Today 14 (2009) 278–283.